Effects of variable material properties in coldwater convection

Daisuke Noto [*]
Faculty of Engineering, Hokkaido University, Sapporo 060-8628, Japan and Department of Earth and Environmental Science, University of Pennsylvania, Philadelphia, Pennsylvania 19104, USA

Hugo N. Ulloa
Department of Earth and Environmental Science, University of Pennsylvania, Philadelphia, Pennsylvania 19104, USA

(Received 29 October 2025; accepted 6 May 2026; published 3 June 2026)

Thermally driven flows have been extensively studied using the canonical Oberbeck-Boussinesq (OB) approximation, which treats material properties as constant except for the buoyancy force, where small density variations are fundamental to driving motion. Yet the validity of this approximation in coldwater systems remains largely unexplored. In such environments, density variations associated with a given temperature difference are relatively small due to the nonlinear equation of state. In contrast, variation in dynamic viscosity and thermal conductivity remains moderate, comparable to those in warmer systems. Here we numerically investigate the effects of temperature-dependent material properties in two canonical configurations of ice-bounded waterbodies: horizontal and vertical convection. Our results show that variable material properties remain dynamically important and significantly affect global transport quantities in quasi-steady states. In particular, we identify anomalous dynamics under specific conditions, in which the dominance of cold and warm circulations completely reverses. This anomaly leads to up to $O(10\%)$ of over- or underestimation in global quantities, including the water-to-ice heat flux, which controls systems' energy and ice melt rates. Although the relative importance of the variable material properties depends on domain size and boundary conditions, their persistent influence in both local dynamics and global quantities underscores their non-negligible and, sometimes, pivotal effects in cold aquatic systems. We therefore conclude that the conventional OB approximation may lead to misinterpretation of the dynamics of cryospheric water bodies by excessively simplifying the underlying thermophysical variability.

DOI: 10.1103/77tz-mg44

I. INTRODUCTION

Inland waterbodies in cryospheric and polar environments are often ice-bounded. Examples include supra-, sub-, and proglacial and seasonally ice-covered lakes [1]. Convective dynamics in such cold waterbodies are of great interest for their role in biogeochemical cycles as well as for their contribution as heat reservoirs on Earth, controlling the ice mass balance [2–4]. It is common to model such convective dynamics using the Oberbeck-Boussinesq (OB) approximation [5,6], assuming that the density fluctuations $\Delta\rho$ produced in the system of interest are small enough

[*]Contact author: dnoto@eng.hokudai.ac.jp

compared with its reference density ρ_r to account for the compressibility and inertia of fluid and so are the material properties, i.e., $\Delta\rho \ll \rho_r$. The OB approximation is therefore traditionally accompanied by constant material properties. Although the OB approximation substantially simplifies the mathematical problem, governed by only two key parameters, the Prandtl number and Rayleigh number, it has been shown to "reasonably" capture the essential physics of convective flows [7], and therefore, it is widely employed.

But to what extent is this approximation reliable? The limit of the OB approximation for water has been discussed specifically in the context of Rayleigh-Bénard convection—the paradigmatic problem of natural convection within a fluid layer heated from below and cooled from above—while accounting for large temperature differences for given material properties [8–12]. The consequence is often called the "non-Oberbeck-Boussinesq (NOB) effect," which manifests as a significant shift of the bulk mean temperature of the convective system, mainly because of the asymmetry of the boundary layer thicknesses caused by the temperature-dependent viscosity. Unlike such environments exposed to large temperature differences $\Delta T = O(10\text{–}100\,\text{K})$, which we may find in engineering systems, temperature variations in cold aquatic systems appear to be much smaller $\Delta T = O(1\ \text{K})$ [13–15].

Cold freshwaters have a characteristic equation of state (EoS) exhibiting a nonmonotonic relationship between density and temperature, where density decreases with the increase of temperature from its maximum ρ_{max} above the temperature of maximum density $T_{\text{md}} = 3.98\,^{\circ}\text{C}$, whereas density increases with temperature between freezing point $T_{\text{fp}} = 0\,^{\circ}\text{C}$ and T_{md}. Owing to this nonmonotonic behavior around the density extremum, temperature difference ΔT around T_{md} results in much smaller density anomalies than those at high temperatures. In contrast, the sensitivities of the dynamic viscosity μ and the thermal conductivity k to temperature changes are greater in this temperature range than at higher temperatures, suggesting that the OB approximation, with constant material properties, may fail. In fact, early numerical works accounting for variable material properties in the context of cold water convection in a cavity [16,17] showcased differences in heat transport and convective dynamics from those with constant material properties [18,19], and the former are more consistent with the experimental results [20,21]. Recently, the significance of variable material properties in convective flows was pointed out briefly [22]. Yet, even to date, the majority of literature has dealt with constant material properties following the classical Boussinesq approximation [23–31], keeping the effects of variable material properties on convection still obscured.

The complex and intertwined fluid dynamics observed in field and laboratory experiments often make the role of temperature-dependent material properties vague. Here we isolate and investigate their influence on convective flows in ice-bounded waterbodies using numerical experiments with "virtual waters," whose thermophysical properties can be systematically tuned. To address this unsolved problem, we focus on two fundamental and distinct convective dynamics. The first is the horizontal convection (HC), in which the fluid surface is exposed to differential heating and cooling [32–34]. This configuration serves as a canonical model for partially ice-covered waterbodies, such as seasonally ice-covered lakes, by imposing $0\,^{\circ}\text{C}$ along part of the surface. The second is vertical convection (VC), where the sidewalls are differentially heated and cooled [35,36]. This setup represents a simplified model of ice-bounded waterbodies, such as proglacial lakes, by setting one vertical wall to be $0\,^{\circ}\text{C}$. The latter two examples from natural systems are shown together with the schematic in Figs. 1(a) and 1(b), respectively.

The paper is structured as follows. Section II presents the conceptual model along with its numerical implementation. Section III reports the results for both horizontal and vertical convection, highlighting how temperature-dependent material properties influence the convective dynamics and the global quantities, such as the bulk mean temperature and the net heat flux from water to ice. Section IV discusses these findings, with particular emphasis on the emergence of anomalous convective dynamics. Finally, Sec. V summarizes the key conclusions and future research directions.

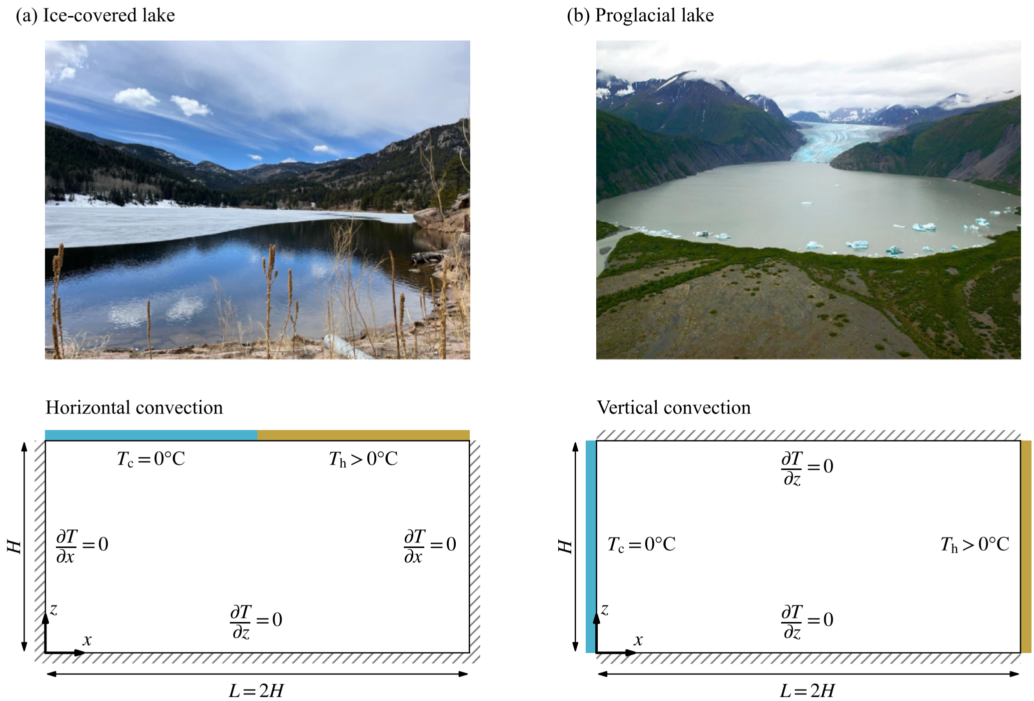

FIG. 1. Cryospheric ice-bounded waterbodies: (a) Partially ice-covered lake, Lake Isabel, Colorado, USA (Photo Credit: Kinetic faith, Shutterstock, ID 2599772893, Standard License) and its conceptual model, horizontal convection (HC). (b) Proglacial lake, Kenai glacier lake, Alaska, USA (Photo Credit: Steve Hillebrand, U.S. Fish & Wildlife Service, Wikipedia, public domain), and its conceptual model, vertical convection (VC). The schematic represents the numerical setup introduced in Sec. II B.

II. PROBLEM FORMULATION

A. Temperature-dependent material properties

We first discuss how material properties are sensitive to temperature change. Figure 2 shows the temperature-dependent material properties of shallow freshwater, (a) density $\rho(T)$, (b) dynamic

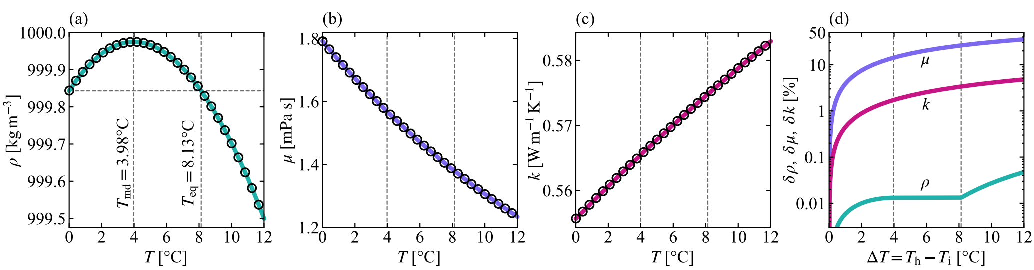

FIG. 2. Temperature-dependent material properties: (a) density $\rho(T)$, (b) dynamics viscosity $\mu(T)$, and (c) thermal conductivity $k(T)$. Scatter plots are the thermophysical properties database from NIST [37], and solid lines are the polynomial fittings [Eq. (3)] used in this study. Variations of material properties for given temperature differences $\Delta T = T_h - T_i$ relative to reference values are shown in (d). Vertical dashed lines correspond to the temperature of the maximum density $T_{md} = 3.98\,°C$ and the ice-water-interface-equivalent temperature $T_{eq} = 8.13\,°C$, i.e., $\rho(T_i) = \rho(T_{eq})$.

viscosity $\mu(T)$, and (c) thermal conductivity $k(T)$. Scatter plots are thermophysical properties obtained from the National Institute of Standards and Technology (NIST) [37], and solid lines are the least-squares fitting to be explained later in detail. Density ρ increases with temperature until T_{md} (dashed line) and decreases monotonically beyond T_{md}. Unlike the latter nonmonotonic behavior of ρ, dynamic viscosity μ decreases and thermal conductivity k increases with temperature. We evaluate the anomalies of each property relative to the corresponding reference value, which are defined as

$$\delta\rho = \frac{\Delta\rho_{\mathrm{max}}}{\rho_{\mathrm{r}}}, \quad \delta\mu = \frac{\Delta\mu_{\mathrm{max}}}{\mu_{\mathrm{r}}}, \quad \text{and} \quad \delta k = \frac{\Delta k_{\mathrm{max}}}{k_{\mathrm{r}}}. \tag{1}$$

Here $\Delta\rho_{\mathrm{max}}$, $\Delta\mu_{\mathrm{max}}$, Δk_{max} represent the maximum difference of each quantity for a given temperature difference imposed on an ice-bounded system, i.e., $\Delta T = T_{\mathrm{h}} - T_{\mathrm{i}}$, where $T_{\mathrm{i}} = 0\,^\circ\mathrm{C}$; we note that the actual value of T_{h} is particularly important as T_{i} is fixed at $0\,^\circ\mathrm{C}$. Because of the nonmonotonicity of ρ, $\Delta\rho_{\mathrm{max}} \neq |\rho(T_{\mathrm{h}}) - \rho(T_{\mathrm{i}})|$ but changes the definition depending on T_{h} [38], that is,

$$\Delta\rho_{\mathrm{max}} = \begin{cases} \rho_{\mathrm{h}} - \rho_{\mathrm{i}} & \text{if } T_{\mathrm{i}} \leqslant T_{\mathrm{h}} < T_{\mathrm{md}} \\ \rho_{\mathrm{max}} - \rho_{\mathrm{i}} & \text{if } T_{\mathrm{md}} \leqslant T_{\mathrm{h}} < T_{\mathrm{eq}} \\ \rho_{\mathrm{max}} - \rho_{\mathrm{h}} & \text{if } T_{\mathrm{eq}} \leqslant T_{\mathrm{h}} \end{cases}, \tag{2}$$

where ρ_{h} is the density at the hot boundary, $\rho_{\mathrm{h}} = \rho(T_{\mathrm{h}})$, and $T_{\mathrm{eq}} \approx 8.13\,^\circ\mathrm{C}$ is the ice-water-interface-equivalent temperature, i.e., $\rho(T_{\mathrm{eq}}) = \rho(T_{\mathrm{i}})$. Conversely, $\Delta\mu_{\mathrm{max}} = |\mu(T_{\mathrm{i}}) - \mu(T_{\mathrm{h}})|$ and $\Delta k_{\mathrm{max}} = |k(T_{\mathrm{i}}) - k(T_{\mathrm{h}})|$ since these two properties monotonically change with temperature as shown in Figs. 2(b) and 2(c). For the reference values, we take those at T_{md}. Figure 2(d) illustrates the relative anomalies of these three quantities. As expected, $\delta\rho$ is approximately 0.01% until $\Delta T \approx 8\,^\circ\mathrm{C}$ and increases with ΔT but remains small, supporting the conventional OB approximation that neglects the effects of density fluctuations except for the buoyancy force. In contrast, $\delta\mu$ and δk are orders of magnitude higher than $\delta\rho$: $\delta\mu$ increases up to $\approx 10\%$ and δk to $\approx 1\%$ within the range of ΔT plotted here. The high sensitivities of μ and k to temperature change warrant consideration of the temperature-dependent material properties in thermally driven flows of cold waters.

Various expressions have been proposed, in particular, to model the nonlinear EoS of cold freshwater. The simplest approach is the linear form, $\rho(T) = \rho_{\mathrm{max}}[1 - \alpha(T - T_{\mathrm{md}})]$ with the negative thermal expansion coefficient α in units of degrees C^{-1}. This simplistic form neglects the nonlinearity of EoS by limiting the temperature range, typically below $2\,^\circ\mathrm{C}$ [30,39]. A quadratic form, $\rho(T) = \rho_{\mathrm{max}}[1 - \alpha(T - T_{\mathrm{md}})^2]$ with the quadratic thermal expansion coefficient α in the units of degrees C^{-2}, is popularly employed for its practicality in representing EoS for $T \lesssim 8\,^\circ\mathrm{C}$ [24,27,29,40]. Otherwise, a different exponent $q < 2$ has often been employed, e.g, $\rho(T) = \rho_{\mathrm{max}}[1 - \alpha|T - T_{\mathrm{md}}|^q]$ with $q \approx 1.895$ and the modified thermal expansion coefficient α in units of degrees C^{-q}, to further extend the applicable temperature range [21,41,42]. These approaches reduce the number of control variables and thus have been utilized to nondimensionalize equations of motion. However, we emphasize that these efforts taken for nondimensionalization may not be meaningful if the system under investigation has a specific temperature that is always imposed—$T_{\mathrm{i}} = 0\,^\circ\mathrm{C}$ in the ice-bounded freshwater system. This constraint makes the system unscalable, forcing us to work with dimensions. Accordingly, we employed high-order polynomial fitting instead of utilizing the aforementioned simplified models to represent the actual temperature dependency as best as possible.

High-order polynomial representations have been used previously, including third-order [26], fourth-order [17], and fifth-order and higher fits [8,9,24,43,44]. Notably, increasing the polynomial order does not complicate the numerical implementation. We, therefore, employed fifth-order polynomial functions for all material properties:

$$\rho(T) = \sum_{i=0}^{5} a_i (T - T_{\mathrm{md}})^i, \tag{3a}$$

$$\mu(T) = \sum_{i=0}^{5} b_i (T - T_{\mathrm{md}})^i, \tag{3b}$$

$$k(T) = \sum_{i=0}^{5} c_i (T - T_{\mathrm{md}})^i. \tag{3c}$$

This formulation allows forcing the maximum density $\rho_{\max}$ to be exactly at T_{md}. Thus, $a_0 = \rho_{\max} = \rho(T_{\mathrm{md}})$, $b_0 = \mu(T_{\mathrm{md}})$, and $c_0 = k(T_{\mathrm{md}})$. The coefficients (provided in Appendix A) are obtained through the least-squares fitting for the freshwater material properties obtained from NIST [37] as shown in the solid lines in Figs. 2(a)–2(c). These fittings provide mean absolute errors of $O(10^{-6}\,\mathrm{kg\,m^{-3}})$ for density, $O(10^{-9}\,\mathrm{Pa\,s})$ for dynamic viscosity, and $O(10^{-8}\,\mathrm{W\,m^{-1}\,{}^{\circ}C^{-1}})$ for thermal conductivity within the temperature range shown in Fig. 2, ensuring accurate representation of actual material properties.

B. Numerical implementation

We performed a two-dimensional (2D) direct numerical simulation (DNS) for the setups of HC and VC schematized in Fig. 1. As does the conventional OB approximation, we assume water to be incompressible and neglect the density variation except for the buoyancy term, but we allow temperature dependency of the other material properties. Since we focus on coldwater systems, the nonlinear EoS [Eq. (3a)] is employed for all cases. Accordingly, the thermo-fluid dynamics is governed by the continuity, momentum, and heat equations (e.g., [9]):

$$\nabla \cdot \boldsymbol{u} = 0, \tag{4a}$$

$$\rho_{\mathrm{r}}\left[\frac{\partial \boldsymbol{u}}{\partial t} + (\boldsymbol{u}\cdot\nabla)\boldsymbol{u}\right] = -\nabla p + \nabla\cdot(\mu[\nabla\boldsymbol{u} + (\nabla\boldsymbol{u})^{\top}]) - \rho g\hat{\boldsymbol{z}}, \tag{4b}$$

$$\rho_{\mathrm{r}}\, C\left[\frac{\partial T}{\partial t} + (\boldsymbol{u}\cdot\nabla)T\right] = \nabla\cdot(k\nabla T). \tag{4c}$$

Here ρ_{r} is the reference, and we use $\rho_{\mathrm{r}} = \rho_{\max}$ for all conditions, and C is the specific heat capacity. Recall that $\mu(T)$ and $k(T)$ are both temperature-dependent and thus space- and time-dependent. Note that, over the temperature range $0 \leqslant T \leqslant 10\,^{\circ}\mathrm{C}$, C exhibits much weaker temperature dependence than the other two quantities. We therefore treat it as constant for simplicity. To characterize the effect of the temperature-dependent material properties, we also perform simulations under the OB-type approximation, in which μ and k are treated as constants, whereas $\rho(T)$ is represented by a fifth-order polynomial fit

$$\nabla \cdot \boldsymbol{u} = 0, \tag{5a}$$

$$\rho_{\mathrm{r}}\left[\frac{\partial \boldsymbol{u}}{\partial t} + (\boldsymbol{u}\cdot\nabla)\boldsymbol{u}\right] = -\nabla p + \mu_{\mathrm{r}}\nabla^2\boldsymbol{u} - \rho g\hat{\boldsymbol{z}}, \tag{5b}$$

$$\rho_{\mathrm{r}}\, C\left[\frac{\partial T}{\partial t} + (\boldsymbol{u}\cdot\nabla)T\right] = k_{\mathrm{r}}\nabla^2 T. \tag{5c}$$

To evaluate the effects of variable material properties properly, we utilize reference values for μ_{r} and k_{r} at the average temperature of the boundaries, i.e., $T_{\mathrm{r}} = (T_{\mathrm{c}} + T_{\mathrm{h}})/2$.

Planning in future laboratory-scale experiments to explore this problem, the height-to-length aspect ratio of the domain is fixed at 2, i.e., $L = 2H$, as schematized in Fig. 1, and we vary H. As a common setup, velocity boundary conditions are no-slip at all boundaries. For the case of HC, the thermal boundary condition at the top ($z = H$) is

$$T(x \leqslant L/2, z = H) = T_{\mathrm{i}} \quad \text{and} \quad T(x > L/2, z = H) = T_{\mathrm{h}}, \tag{6}$$

and all other boundaries are set to be adiabatic, i.e., $\partial T/\partial n = 0$. For numerical stability, the surface boundary condition is implemented using a continuous function with a smooth and short transition length $d \ll L$ at $x = L/2$ from T_{i} to T_{h}:

$$T(x, z = H) = T_{\mathrm{i}} + \frac{T_{\mathrm{h}} - T_{\mathrm{i}}}{2}\left[\tanh\left(\frac{x - L/2}{d}\right) + 1\right]. \tag{7}$$

We here consistently use $d = 4$ mm for all cases, with $d/L \ll 1$. For the case of VC, the left and right walls are at constant and different temperatures,

$$T(x = 0, z) = T_{\mathrm{i}} \quad \text{and} \quad T(x = L, z) = T_{\mathrm{h}}, \tag{8}$$

whereas all other boundaries are set to be adiabatic, i.e., $\partial T/\partial n = 0$.

Note that we can define the classic dimensionless parameters using the maximum density difference $\Delta\rho_{\mathrm{max}}$ and the material properties at the reference temperature T_{r}. The Rayleigh number Ra, the ratio of the destabilizing buoyancy force to the viscous and thermal dissipation, is defined as

$$\mathrm{Ra} = \frac{\Delta\rho_{\mathrm{max}}\, g H^3}{\rho_{\mathrm{r}}\, \nu_{\mathrm{r}}\, \kappa_{\mathrm{r}}}, \tag{9}$$

where $\nu_{\mathrm{r}} = \mu_{\mathrm{r}}/\rho_{\mathrm{r}}$ is the kinematic viscosity and $\kappa_{\mathrm{r}} = k_{\mathrm{r}}/(\rho_{\mathrm{r}} C)$ is the thermal diffusivity at T_{r}. The Prandtl number Pr, the ratio of momentum to thermal diffusivities, is defined as $\mathrm{Pr} = \nu_{\mathrm{r}}/\kappa_{\mathrm{r}}$. Taking $T_{\mathrm{r}} = T_{\mathrm{md}}$, Pr is always $\mathrm{Pr} = 11.7$, yet Ra varies order of magnitudes—here it ranges in $O(10^3$–$10^8)$ for $1\,^\circ\mathrm{C} \leqslant T_{\mathrm{h}} \leqslant 10\,^\circ\mathrm{C}$ and $10 \text{ mm} \leqslant H \leqslant 200$ mm. We here remark that although these nondimensional parameters can be computed for a given temperature condition, the same value of Ra achieved at different temperature conditions does not ensure the same physics; Ra is invariant when $T_{\mathrm{md}} \leqslant T_{\mathrm{h}} \leqslant T_{\mathrm{eq}}$ as $\Delta\rho_{\mathrm{max}} = \rho_{\mathrm{md}} - \rho_{\mathrm{i}}$ [Eq. (2)], but the convective dynamics differ completely as shown later. The latter indicates the need for additional dimensionless parameters concerning the nonlinearity of EoS for generalization—as some previous work did [26,29,45]. However, since we specifically work on cold waters, such an effort makes no physical sense as the EoS is unique only for water. Therefore, we hereafter describe the fluid physics of cold waters based on the actual control parameters, T_{h} and H [46]. We further provide the relationship between Ra and the control parameters T_{h} and H in Appendix B.

The second-order central difference scheme on the staggered grid is employed for spatial discretization [47], and the time marching is the first-order explicit Euler scheme, satisfying the Courant-Friedrichs-Lewy (CFL) condition, i.e., $\mathrm{CFL} < 0.1$ (typically, $\mathrm{CFL} < 0.05$). The simplified marker and cell (SMAC) scheme is adopted to solve the pressure Poisson equation [48]. Numerical implementation is done in Python [the code is publicly available from [49]]. The spatial resolution is chosen to resolve the smallest length scale of the system, i.e., the Batchelor scale, $\eta_{\mathrm{B}} \approx O(10^{-3}\text{ m})$, smaller than the Kolmogolov scale $\eta_{\mathrm{K}} = \mathrm{Pr}^{1/2}\,\eta_{\mathrm{B}}$ as $\mathrm{Pr} > 1$. The latter criterion is met through an *a posteriori* check suggested in [50]; the smallest η_{B} was $\approx$1.5 mm in the parameter range here investigated, and the spatial resolution was 1 mm for all the cases. To resolve these scales and for the computational limits, the system length scale H is equal to or lower than 200 mm, relevant for tabletop laboratory experiments, yet the consequential dynamics are expected not to differ significantly for larger scale systems. It is important to simulate the systems without introducing any closure models for effective diffusivities in order to evaluate the effects of variable material properties. We next discuss the (statistically) steady states in Sec. III.

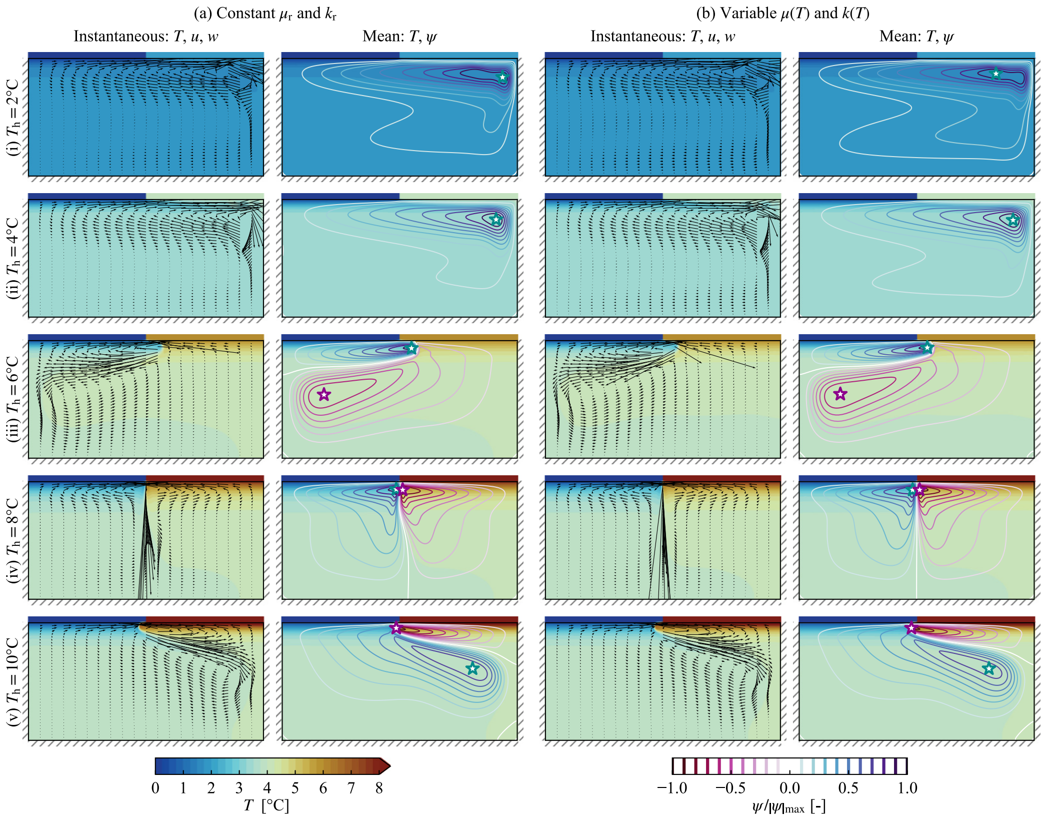

FIG. 3. Steady-state flow fields of horizontal convection with $H = 200$ mm for (a) constant material properties μ_r and k_r and (b) variable material properties $\mu(T)$ and $k(T)$. Different temperatures on the hot boundaries T_h are shown from top to bottom: (i) $T_h = 2$ °C, (ii) 4 °C, (iii) 6 °C, (iv) 8 °C, and (v) 10 °C. The left column shows snapshots, temperature fields (background color), and velocity vectors (arrows), and the right column shows time averages, temperature fields (background color), and streamfunction fields (colored contours). The locations of the maximum and minimum of the streamfunction fields are marked by star symbols.

III. RESULTS

A. Horizontal convection

We first look at the cases of HC, schematized in Fig. 1(a), to discuss the phenomenology of an analog system for partially ice-covered aquatic bodies. Figure 3 showcases the steady-state flow fields for the case of $H = 200$ mm at different temperature conditions on the hot boundary (upper right side of the domain). The results of constant material properties are shown in Fig. 3(a), and those of variable properties in Fig. 3(b). Each showcases instantaneous and mean flow fields under quasi-steady states. On the instantaneous fields, color contours represent temperature fields, and the superposed arrows are velocity vectors. On the mean fields, color contours represent temperature distributions, and the superposed contour lines are streamfunction fields (see Appendix C for the computational method) where blue and red lines correspond to clockwise (CW) and counterclockwise (CCW) circulations, respectively. The system undergoes different flow regimes by changing T_h, even though Ra varies only slightly among the conditions. For $T_h \lesssim T_{md}$ [Figs. 3(i) and 3(ii)], the system reproduces the so-called stratified horizontal convection [51,52]. The cold but light fluid from the ice surface pushes the denser fluid on the hot surface downward, driving a CW overturning circulation that partially penetrates the deeper stable layer. A drastic change manifests when $T_h > T_{md}$ as shown in Fig. 3(iii). Unlike a single CW overturning circulation taking place for $T_h \lesssim T_{md}$, another CCW circulation coemerges. The latter double circulations can be explained by the cabbeling phenomenon; a downward flow is generated when colder $T < T_{md}$ and warmer $T > T_{md}$ waters meet at the center, dividing the domain into two circulations. The original CW circulation is now severely confined right beneath the ice surface as the CCW circulation crawls underneath it. The newly emerged circulation distributes the warm waters laterally, but the cold CW circulation protects the ice surface from being exposed to such a high heat content. When $T_h = 8\,^{\circ}\mathrm{C}$ [Fig. 3(iv)], two circulations are almost balanced, as is evident from the streamfunction fields with the common structures. The horizontal density difference is negligibly small in this case as $\rho(T = 8\,^{\circ}\mathrm{C}) \approx \rho_i$, and only the cabbeling is the driving mechanism of the circulations. The sharp top-to-bottom separation induced by the opposing circulation cells across the horizontal domain closely resembles the thermal bar phenomenon commonly observed in coastal waters, where density-driven circulation reverses across the temperature of maximum density, T_{md}, due to the formation of a lateral density front [53–55]. Finally, when $T_h = 10\,^{\circ}\mathrm{C}$ [Fig. 3(v)], the cold CW circulation dominates the system, a left-right-flipped analog of $T_h = 6\,^{\circ}\mathrm{C}$ [Fig. 3(iii)]. The cold waters are distributed laterally beneath the warm CCW circulation confined within the shallow region.

A key takeaway from Fig. 3 is that, although present, the effect of variable material properties is not strong enough to produce visually identifiable differences in the convective dynamics.

B. Vertical convection

Now let's shift our attention to the phenomenology of VC, an analog system for proglacial lakes as schematized in Fig. 1(b). In the same manner as Fig. 3 for HC, the steady-state flow fields for the case of $H = 200$ mm at different temperature conditions on the hot boundary (right side of the domain) are showcased in Fig. 4: (a) instantaneous flow fields and (b) mean flow fields. For the low-temperature conditions $T_h \lesssim T_{md}$ [Figs. 4(i) and 4(ii)], a single CW overturning circulation takes place all over the domain, as the cold boundary produces the least dense water flowing upward, whereas the hot boundary holds the densest water plunging down. Note that, although they are not visible in Fig. 4, the vertical flows are present while being strongly confined on the side walls. However, once T_h exceeds T_{md} [Fig. 4(iii)], a small CCW circulation emerged locally at the lower right corner of the domain. This may also be a consequence of the cabbeling dynamics: The warm water on the hot boundary is positively buoyant, but it plunges down when it meets the incoming cold water from the left because of the peak density at T_{md}, resulting in a hot water pocket at the bottom of the right boundary. The emergence of these two circulations has been previously reported both numerically and experimentally for a (real) ice—phase-changing—boundary for the cold wall [56,57]. A striking difference between the constant and variable properties is finally seen for $T_h = 8\,^{\circ}\mathrm{C}$ [Fig. 4(iv)]. For the constant property, as expected, the CCW circulation grows laterally and takes approximately half of the domain, resulting in roughly symmetric structures, akin to those in HC [Fig. 3(iv)]. These symmetric two circulations have been reported in previous works utilizing constant material properties [58–60]. However, when the variable properties are in effect, the CCW circulation completely governs the system, and the CW circulation is aggressively constrained to the cold boundary. The entire system is now much warmer than the case with constant properties. These asymmetric two circulations have also been reported in [17], which account for the variable material properties. When $T_h = 10\,^{\circ}\mathrm{C}$ [Fig. 4(v)], however, the latter distinctive difference diminishes: The CCW circulation occupies most of the entire domain, while the cold surface produces the wedgelike CW circulation for both cases. The cold water pocket in this condition is the left-right flipped analog of the warm one shown in Fig. 4(iii).

Unlike HC, a pronounced difference manifests for $T_h = 8\,^{\circ}\mathrm{C}$ for the case of VC as shown in Fig. 4(d). That is, the effect of variable material properties is strong enough to be recognized, and consequently, we expect its substantial influence on the global quantities we analyze next.

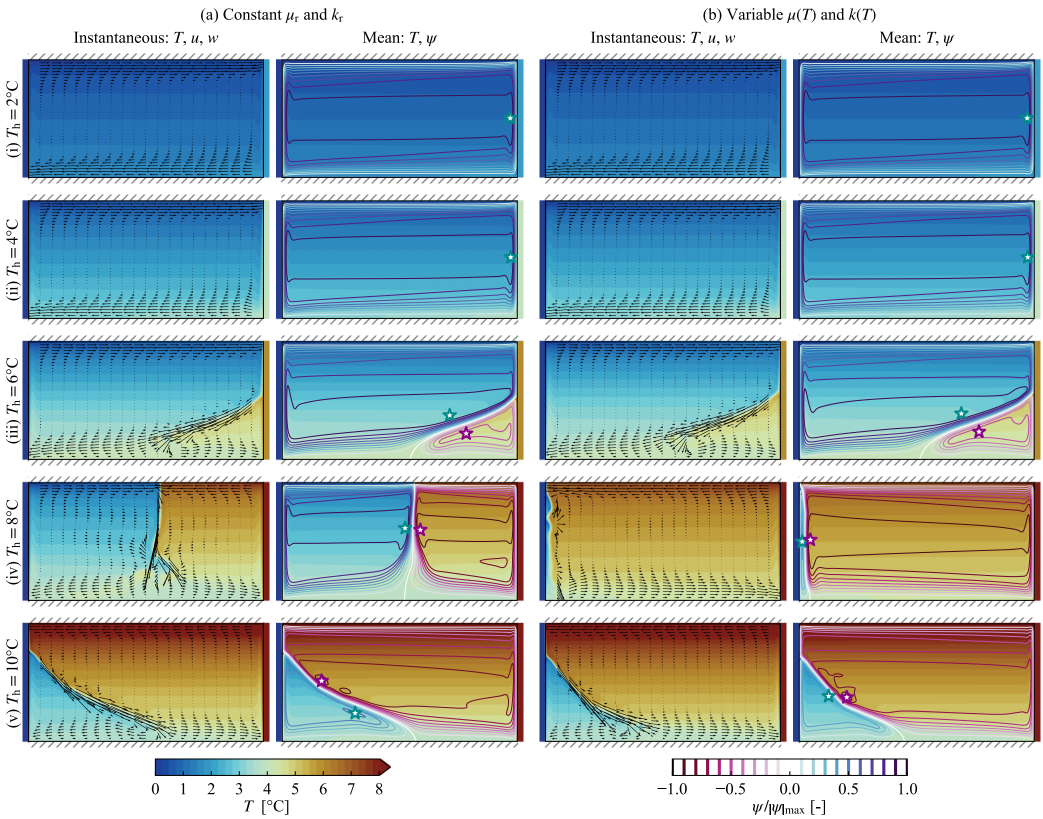

FIG. 4. Steady-state flow fields of vertical convection with $H = 200$ mm for (a) constant material properties μ_r and k_r and (b) variable material properties $\mu(T)$ and $k(T)$. Different temperatures on the hot boundaries T_h are shown from top to bottom: (i) $T_h = 2\,°C$, (ii) $4\,°C$, (iii) $6\,°C$, (iv) $8\,°C$, and (v) $10\,°C$. The left column shows snapshots, temperature fields (background color), and velocity vectors (arrows), and the right column shows time averages, temperature fields (background color), and streamfunction fields (colored contours). The locations of the maximum and minimum of the streamfunction fields are marked by start symbols.

C. Effects of temperature-dependent material properties

We further quantify the effects of temperature-dependent material properties by examining global quantities. Recall that the cases with constant material properties utilized the average temperature of the cold and the hot boundaries as the reference temperature, i.e., $T_r = (T_c + T_h)/2$ for fair comparisons. Here we focus on four quantities relevant for characterizing aquatic systems: the bulk mean temperature, the water-to-ice heat transport, the mass transport, and the total kinetic energy. The bulk mean temperature $\langle T\rangle$ in unit of degrees C is simply defined as an average over the 2D domain and time,

$$\langle T\rangle = \frac{1}{HL\mathcal{T}}\int_t^{t+\mathcal{T}}\int_0^H\int_0^L T(x,z,t)\,\mathrm{d}x\,\mathrm{d}z\,\mathrm{d}t, \tag{10}$$

where $\mathcal{T}$ is the arbitrary time window at quasi-steady state. For the water-to-ice heat transport, we consider the average heat transport along the ice boundaries ϕ_{wi} in the unit of W m^{-2}, and thus it is defined separately for HC and VC: For the case of HC, it is the vertical heat flux at $0 \leqslant x \leqslant L/2$ and $z = H$,

$$\phi_{wi} = \frac{2}{L\mathcal{T}}\int_t^{t+\mathcal{T}}\int_0^{L/2}\left[-k(x,H,t)\,\frac{\partial T}{\partial z}(x,H,t)\right]\mathrm{d}x\,\mathrm{d}t, \tag{11}$$

and for the case of VC, it is the horizontal heat flux at $x = 0$ and $0 \leqslant z \leqslant H$,

$$\phi_{\mathrm{wi}} = \frac{1}{H\mathcal{T}} \int_t^{t+\mathcal{T}} \int_0^H \left[-k(0, z, t) \frac{\partial T}{\partial x}(0, z, t) \right] \mathrm{d}z\, \mathrm{d}t. \tag{12}$$

For the mass transport, we evaluate the maximum streamfunction ψ_{max} of the cold CW circulation adjacent to the ice boundary as it formed for all conditions, regardless of T_{h}. We first compute a mean streamfunction field ψ, following the method described in detail in Appendix C, from the mean vorticity fields at the quasi-steady states, and obtain its maximum ψ_{max} in units of $\mathrm{m}^2\ \mathrm{s}^{-1}$. The total kinetic energy E_{k} is defined as the integration of the kinetic energy density $\mathcal{E}_{\mathrm{k}} = \rho_{\mathrm{r}}(u^2 + w^2)$:

$$E_{\mathrm{k}} = \frac{1}{\mathcal{T}} \int_t^{t+\mathcal{T}} \int_0^H \int_0^L \mathcal{E}_{\mathrm{k}}(x, z, t)\, \mathrm{d}x\, \mathrm{d}z\, \mathrm{d}t. \tag{13}$$

E_{k} and $\mathcal{E}_{\mathrm{k}}$ are computed in units of J and $\mathrm{J\,m}^{-3}$, respectively. To characterize the NOB effect, we quantify the relative error of each quantity, defined as $\delta\langle T\rangle = (\langle T\rangle^{\mathrm{c}} - \langle T\rangle^{\mathrm{v}})/\langle T\rangle^{\mathrm{c}}$, $\delta\phi_{\mathrm{wi}} = (\phi_{\mathrm{wi}}^{\mathrm{c}} - \phi_{\mathrm{wi}}^{\mathrm{v}})/\phi_{\mathrm{wi}}^{\mathrm{c}}$, $\delta\psi_{\mathrm{max}} = (\psi_{\mathrm{max}}^{\mathrm{c}} - \psi_{\mathrm{max}}^{\mathrm{v}})/\psi_{\mathrm{max}}^{\mathrm{c}}$, and $\delta E_{\mathrm{k}} = (E_{\mathrm{k}}^{\mathrm{c}} - E_{\mathrm{k}}^{\mathrm{v}})/E_{\mathrm{k}}^{\mathrm{c}}$, where the superscripts c and v denote constant and variable properties, respectively. That is, the relative errors evaluate the differences from the OB approximation; positive values indicate overestimates by the classic OB approximation, while negative values indicate underestimates. Note that $\delta\langle T\rangle$ is evaluated as absolute temperature; otherwise, the error can be amplified for low-temperature conditions, as $\langle T\rangle$ is close to zero.

Figure 5 shows the summary of these global quantities in HC configurations mapped on the T_{h}-H domain: (a) bulk mean temperature $\langle T\rangle$, (b) water-to-ice heat flux ϕ_{wi}, (c) mass transport ψ_{max}, and (d) kinetic energy E_{k}. From left to right, we show the results of the constant material properties (left), those of the variable material properties (middle), and the relative errors (right). The scatter plots, colored by each quantity, represent data explored by DNS, and the background contours are the interpolations for the sake of visualization. The symbols represent the flow states; the circles are for fully steady states, and the diamonds are for unsteady states in which the quantities are computed for their statistically steady states. The vertical dashed lines indicate T_{md} (left) and T_{eq} (right). As a general trend for $\langle T\rangle$, it increases with the increase of T_{h} regardless of H. The relative errors stay small, $\lesssim \pm 0.04\%$, for all conditions. This is expected from the almost consistent convective flow structures showcased in Fig. 3. The errors tend to be larger for the smaller domain size, regardless of T_{h}. The latter trend appears to be reasonable because the smaller domain can drive more diffusive flow conditions, which can directly be influenced by the change of material properties. The same explanation applies to the water-to-ice heat flux shown in Fig. 5(b). The effect of variable material properties (mostly the thermal conductivity) is prominent for the smaller domain, recording the errors of $O(10\%)$, while those in the larger domains remain small. Similar trends are also seen for ψ_{max} and E_{k}, and the errors can go up to $O(10\%)$. Despite the relatively large errors for the smaller domains, the larger domains, which are more relevant for the practical laboratory or geophysical applications, do not grow with the size.

In the same manner, Fig. 6 shows the summary of the global quantities in VC configurations. As a prominent trend, large errors are observed primarily for $T_{\mathrm{h}} = 8\,^{\circ}\mathrm{C}$. The mean temperature $\langle T\rangle$ is substantially underestimated for the latter case compared to the maximum errors for HC [Fig. 5(a)]. The other quantities are also mispredicted, specifically for $T_{\mathrm{h}} = 8\,^{\circ}\mathrm{C}$, tied with the anomalous convective dynamics observed in Fig. 4. Similar to $\langle T\rangle$, the errors of the water-to-ice heat flux, the mass transport, and the kinetic energy go up to $\approx$10%, $\approx$60%, and 30%, respectively. Here we highlight that the key difference from HC is the conditions under which we observe large errors. For HC, large errors are observed for smaller domains, as the differences come directly from the conductive heat fluxes imposed on the stabilizing boundaries. In contrast, for VC, large errors are observed for larger domains, which are more relevant to practical applications, as the differences are the consequence of convective dynamics driven by the destabilizing boundaries. Moreover, the

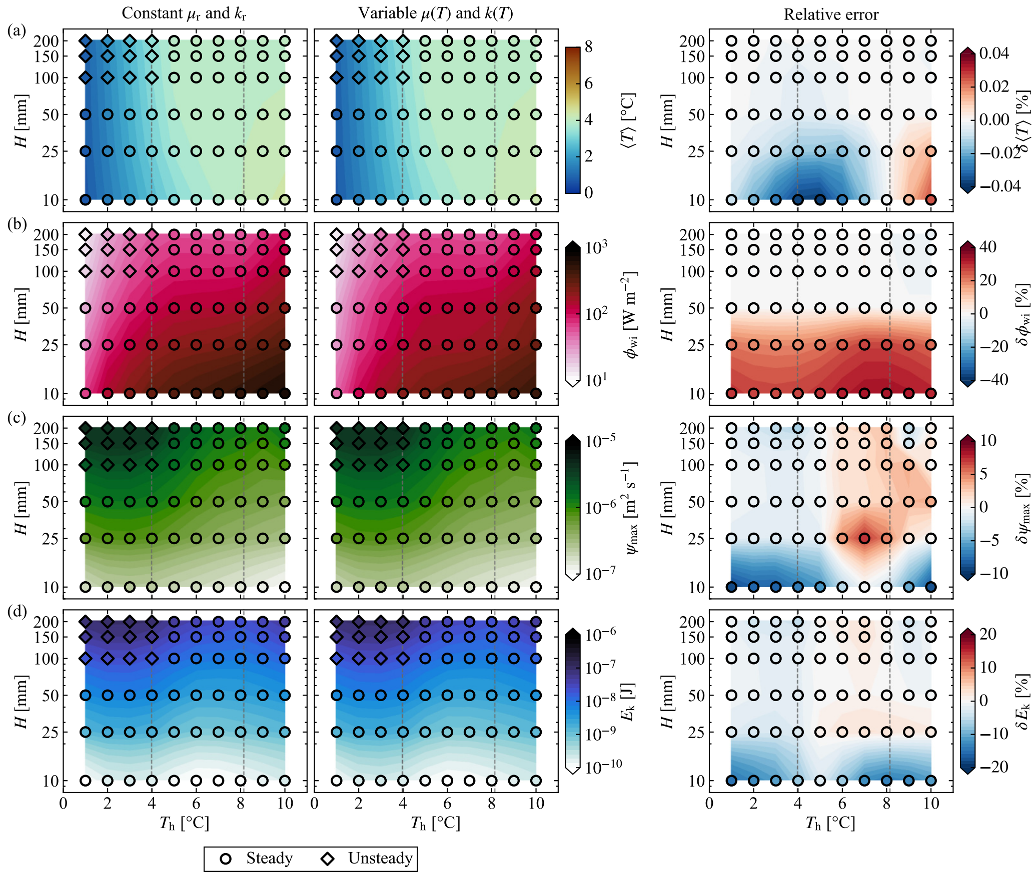

FIG. 5. Effects of temperature-dependent properties on global quantities for HC: (a) bulk mean temperature $\langle T \rangle$; (b) water-to-ice heat transport ϕ_{wi}; (c) mass transport ψ_{max}; and (d) kinetic energy E_k. Left panels show those quantities for the constant material properties (the OB approximation), the middle panels show those for the variable material properties (the NOB condition), and the right panels show the corresponding relative errors. The scatter plots are the points obtained from DNS, and the background colormap represents the interpolation. The circles are fully steady states, and the diamonds are unsteady states, but the quantities are obtained at the statistically steady states.

trend showcased in Fig. 6 suggests that these errors are expected to increase or at least remain large for even larger domains.

In summary, the results shown in Figs. 5 and 6 underscore the non-negligible contributions of variable material properties in the global quantities relevant to characterizing the convective dynamics of the systems, even if the convective dynamics appear macroscopically similar. These significant contributions of the variable material properties have to our knowledge never been reported for water systems with such small temperature differences, yet at higher temperature ranges [11,12].

IV. DISCUSSION

A. Source of anomalies

A fundamental question arising here is: Why is the effect of temperature-dependent material properties specifically evident in particular conditions? Here we delve deeper into the mechanism of

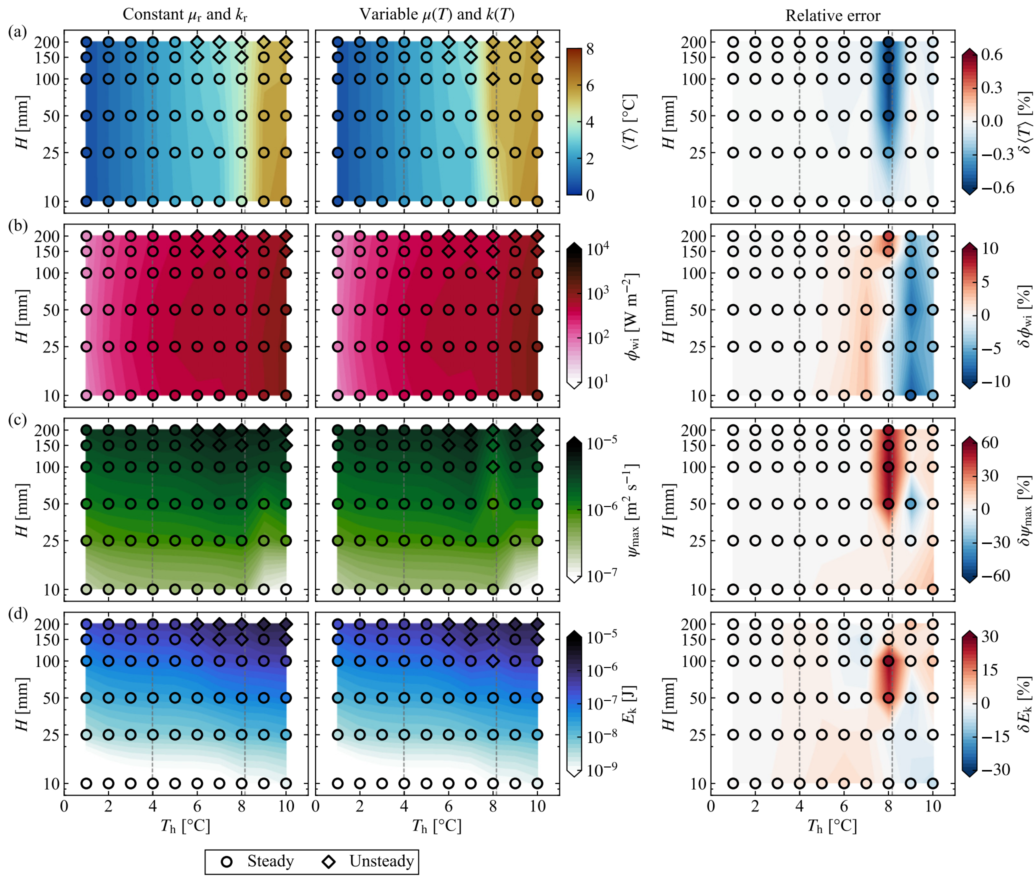

FIG. 6. Effects of temperature-dependent properties on global quantities for VC: (a) bulk mean temperature $\langle T \rangle$; (b) water-to-ice heat transport ϕ_{wi}; (c) mass transport ψ_{max}; and (d) kinetic energy E_k. Left panels show those quantities for the constant material properties (the OB approximation), the middle panels show those for the variable material properties (the NOB condition), and the right panels show the corresponding relative errors. The scatter plots are the points obtained from the DNS, and the background colormap represents the interpolation. The circles are fully steady states, and the diamonds are unsteady states, but the quantities are obtained at the statistically steady states.

the NOB effect by focusing on the conditions for $T_h \approx 8\,°C$ in the VC configuration, those exhibiting remarkable differences in Figs. 4 and 6.

Let's start by identifying which material property, $\mu(T)$ and $k(T)$, essentially leads to the noticeable difference. The numerical implementation [49] is flexible to turn on and off the variable material properties independently for μ and k. Here we first simulated the case with constant material properties until the quasi-steady state was reached. Then its last snapshot is utilized as the initial condition for the cases with temperature-dependent material properties, and they are run until reaching quasi-steady states again. These transient dynamics are summarized in Fig. 7. The mean temperature profiles $\langle T \rangle$ [Fig. 7(a)] display the transition before (shaded period) and after the effect of variable material properties, leading to the increase in $\langle T \rangle$. Although the time required to reach another quasi-steady state differs across the combinations of the variable material properties, all cases eventually attain statistically the same $\langle T \rangle$, higher than that for constant material properties by $\approx$1.5 °C. The time to reach the plateau is approximately 50 h for $\mu(T)$ and $k(T)$, 90 h for $\mu(T)$

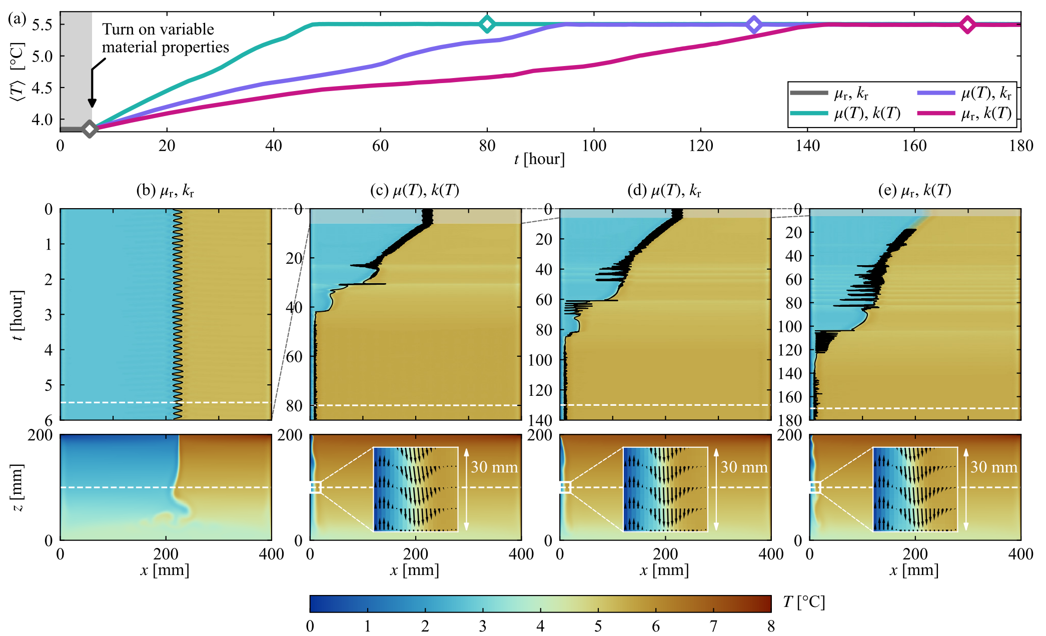

FIG. 7. Transient dynamics from constant to variable material properties in VC with $T_{\mathrm{h}} = 8\,^{\circ}\mathrm{C}$ and $H = 200\,\mathrm{mm}$. (a) Mean temperature profiles $\langle T \rangle$. The shaded period corresponds to that for the constant material properties, and the variable material properties are selectively turned on afterwards. Hovmöller diagram of temperature T obtained at the middle depth $z = H/2 = 100\,\mathrm{mm}$ (middle) and snapshot of temperature field (bottom) for different conditions: (b) μ_{r} and k_{r}, (c) $\mu(T)$ and $k(T)$, (d) $\mu(T)$ and k_{r}, and (e) μ_{r} and $k(T)$. The snapshots correspond to the symbols in (a) and the dashed lines in the Hovmöller diagram. Insets in (c)–(e) showcase the close-up of the vicinity of the wall with the superposition of velocity vectors.

and k_{r}, and 150 h for μ_{r} and $k(T)$. The latter times are in fact at the same order as the thermal diffusion timescale, $\tau_\kappa \approx 80$ h for this configuration. A more detailed view of the temperature evolution for each case is shown in Figs. 7(b)–7(e) as the Hovmöller diagram of T extracted from the middle height $z = H/2$ (top row). Snapshots of the full temperature field at quasi-steady state (bottom row) correspond to the times marked by diamonds in Fig. 7(a) and the dashed lines in the Hovmöller diagrams. The case with constant material properties [Fig. 7(b)] exhibits oscillatory behavior of the downward flow, represented as the black contour line of $T = T_{\mathrm{md}}$, and the cold circulation appears to be slightly larger than the warm one. In all the other cases, however, the warm circulation starts to expand laterally immediately after turning on the variable material properties, as shown by the migration of the contour line of $T = T_{\mathrm{md}}$ toward the cold wall [Figs. 7(c)–7(e)]. The warm circulation eventually dominates almost the whole domain while compressing the cold one onto the cold wall, as shown in the snapshots and the close-up of the ice-wall proximity (insets). Because of the strong shear of the counter circulations induced by the cabbeling, the interface, at $T \approx T_{\mathrm{md}}$, fluctuates. The latter shear-driven instability leads to somewhat periodic undulations that imprint a depth-dependent water-to-ice heat flux along the depth, which may create distinctive patterns called scallops on the ice wall if its phase change is allowed [61].

The results (Fig. 7) demonstrate that both $\mu(T)$ and $k(T)$ contribute to the observed horizontal asymmetry in the convective flow field. Specifically, an increase in local dynamic viscosity or a decrease in thermal conductivity near the cold vertical ice boundary appears to induce similar dynamical effects. These influences are encapsulated by the local Prandtl number, $\mathrm{Pr}(T) = C\,\mu(T)/k(T)$, which represents the ratio of momentum diffusion to thermal diffusion. From the

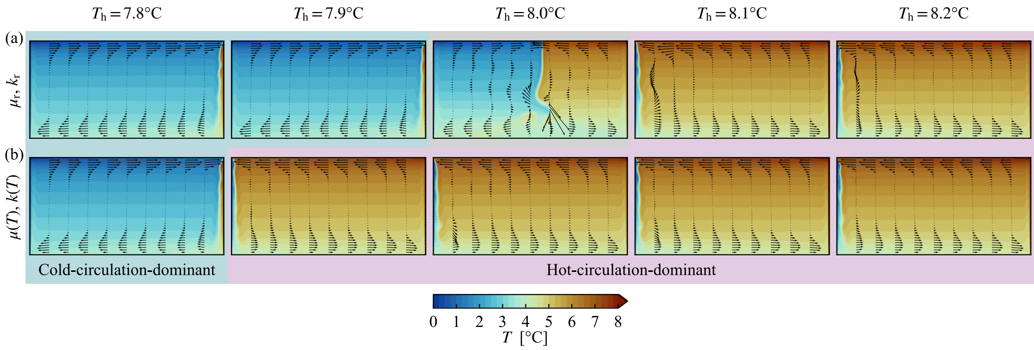

FIG. 8. Instantaneous flow fields of vertical convection at quasi-steady states with $H = 200$ mm for $7.8\,°\mathrm{C} \leqslant T_h \leqslant 8.2\,°\mathrm{C}$: (a) constant material properties and (b) variable material properties.

temperature-dependent behaviors of $\mu(T)$ and $k(T)$ (Fig. 2), both factors contribute to modulate $\mathrm{Pr}(T)$ in the same way; in colder regions, $\mathrm{Pr}(T)$ increases due to enhanced viscosity and reduced thermal conductivity, while it decreases in warmer regions. This fact guides us to hypothesize that spatial variations in $\mathrm{Pr}(T)$ between the cold (left) and hot (right) boundaries yield the horizontal symmetry breaking. For the shown specific configuration, VC with $T_h = 8\,°\mathrm{C}$, the two convective circulations are driven by the destabilizing buoyancy supplied from the two side walls, as well as by cabbeling occurring at the interface of the circulation cells. Thus, cabbeling works as a mass isolator, keeping the two circulations independent from each other. Because of this isolation and the steady-state regime, the mechanical energy budget must be closed within each circulation, i.e., the two side walls keep supplying almost the equivalent destabilizing buoyancy flux through the local available potential energy [62] as $T_h \approx T_{eq} = 8.13\,°\mathrm{C}$. However, the viscous dissipation rate relative to the thermal diffusion rate differs between the cold and hot circulations due to $\mathrm{Pr}(T)$. Even though the supplied destabilizing buoyancy is almost the same, the cold circulation dissipates the produced momentum more rapidly than the hot circulation compared to the thermal diffusion. This imbalance in the energy consumption due to $\mathrm{Pr}(T)$ leads the system to evolve toward an asymmetric equilibrium, a narrower cold circulation, a wider hot circulation [Fig. 4(b-iv)], and consequently, anomalies in the global quantities derived from the whole system (Fig. 6). In other words, we can interpret the NOB effect as a spatial redistribution of the energy partitioning, resulting in an effective augmentation of the destabilizing buoyancy force relative to viscous dissipation.

Conversely, for the cases of HC, the symmetry breaking due to the variable material properties is not as evident as that in VC. The cold and hot boundaries both act as stabilizing surfaces, reinforcing the background stratification, and the only driving mechanism is the cabbeling. The dense fluid directly plunges down from the interface of the two boundaries, and therefore, the two circulations are fully separated geometrically and do not compete with each other for dominance, unlike VC.

B. Specificity of anomalies

The effect of the variable material properties is subtle and not always distinct, even if it exists. This is evident from the narrow range of T_h, $7\,°\mathrm{C} < T_h < 9\,°\mathrm{C}$, showing anomalous peaks in the right panels of Fig. 6. The minor effect of the variable material properties is concealed by the major effect of the differential destabilizing buoyancy originating from the cold and hot boundaries. This result highlights the fact that the anomaly in the convective dynamics happens only when the two destabilizing forces compete while being dissipated. We further specify the anomaly range by running more cases for VC with $T_h \approx 8\,°\mathrm{C}$. Figure 8 showcases the snapshots at quasi-steady state for the range of $7.8\,°\mathrm{C} \leqslant T_h \leqslant 8.2\,°\mathrm{C}$. The notable finding is that there is a sharp transition from the cold-circulation-dominant to the hot-circulation-dominant regimes between $T_h = 7.8\,°\mathrm{C}$

and 7.9 °C for the cases of variable material properties, and the transition is relatively blunt, between $T_\mathrm{h} = 7.9\,^\circ$C and 8.1 °C, for the case of constant material properties. However, we note that the overall trend is essentially the same. The anomalous behaviors in Fig. 6 are understood as specific events happening when comparing two different regimes around the latter transition, which are expected to be more evident for $T_\mathrm{h} = 7.9\,^\circ$C. Because of the highly sensitive nature of the system to the boundary temperature, and the long-term influences of the variable material properties shown in Fig. 7, the systems exhibit anomalous behaviors in both local convective dynamics and global quantities when looking at the quasi-steady state with the same boundary conditions.

C. Validity of the conventional approximation

For most cases, the conventional OB approximation allows for reproducing "perceptually" similar convective dynamics, supporting the validity of the approximation to some extent. However, although the systems we investigated here limit their domain sizes at the laboratory scales, the significant effects of variable material properties appear to persist in global quantities, regardless of the domain size and the boundary temperature configurations (Figs. 5 and 6). Moreover, the high sensitivity to boundary conditions shown in Fig. 8 emphasizes the importance of the actual temperature on the boundary, which cannot be parametrized using the classic OB approximation. This may represent a key conceptual difference that must be considered alongside variable material properties, as the same Ra does not necessarily ensure the same dynamics in coldwater systems (see further discussion in Appendix B). In this context, the actual temperature should be regarded as an additional control parameter [46]. Accordingly, physical interpretations derived from the conventional OB approximation require extra caution when this modeling framework is applied to natural ice-bounded aquatic systems, despite the fact that the approximation has been extensively used. In particular, in the context of global ice mass loss, the misprediction of the water-to-ice heat flux ϕ_wi cascades directly into errors in the predicted ice melt rate; up to $O(10\%)$ of over- or underestimation can be made by the excessive simplification of numerical modeling (Fig. 6). A similar conclusion echos for other global quantities relevant to fisheries, transportation, recreation, and energy production [63–66]. We, therefore, underscore the importance of incorporating variable material properties to better represent thermally driven flows in cold aquatic systems.

V. CONCLUSIONS

We numerically investigated the effects of temperature-dependent material properties—dynamic viscosity and thermal conductivity—on thermally driven flows in coldwater systems, focusing on two canonical setups relevant to ice-bounded aquatic systems: horizontal and vertical convection. The classic Oberbeck-Boussinesq (OB) approximation, which considers constant material properties, is confirmed to hold for most of the conditions examined here. This finding supports the applicability of many previous studies that rely on constant-property models to describe the leading-order dynamics of coldwater convection.

However, we identified a remarkable breakdown of the OB approximation and effects of variable material properties for specific conditions in vertical convection—relevant, for example, to proglacial aquatic system dynamics. Although the latter manifests in a narrow range of thermal boundary conditions, the conventional OB assumptions do not hold, and the system leads to anomalies in both local convective dynamics and global quantities, such as bulk mean temperature, water-to-ice heat flux, mass transport, and kinetic energy. Such anomalous convective dynamics appear to be a consequence of the faster viscous dissipation rate in colder regions compared to the slower thermal dissipation rate caused by the increase in local viscosity and the decrease in local thermal diffusion due to variable material properties in transient states. While our results ensure the validity of many studies that utilize constant material properties, the identified anomaly suggests the need of using a more comprehensive mathematical model that accounts for temperature-dependent material properties and additional control parameters for studies focusing on the convective dynamics of coldwater, governed by a nonlinear EoS. In particular, we warn of the potential misrepresentation of coldwater dynamics due to excessive simplification introduced by conventional models, which sometimes do not align with the actual complexity of cold aquatic systems.

ACKNOWLEDGMENTS

The authors thank Dr. Yuji Tasaka, Dr. Takatoshi Yanagisawa, and Dr. Takehiro Miyagoshi for insightful discussions of the problem. The authors acknowledge the financial supports from the Start-up funding of the University of Pennsylvania and the JST EXPERT-J, Japan Grant No. JPMJEX2511.

DATA AVAILABILITY

The numerical code to reproduce the results in this article is openly available [49].

APPENDIX A: COEFFICIENTS OF POLYNOMIAL FITTING FOR TEMPERATURE-DEPENDENT MATERIAL PROPERTIES

In this study the material properties, ρ, μ, and k are modeled using fifth-order polynomials as formulated in Eq. (3). The obtained coefficients for ρ, μ, and k are provided in Table I.

APPENDIX B: RAYLEIGH NUMBER

We intentionally utilized the dimensional parameters to describe the examined conditions, hot boundary temperature T_{h}, and height H. This is rooted in the unscalable nature of the problem setting [38,46], i.e., the nonmonotonic EoS of cold water (Fig. 2) and the fixed temperature condition on the cold wall, $T_{\mathrm{c}} = T_{\mathrm{i}} = 0\,^{\circ}\mathrm{C}$. Because of these constraints, the maximum density difference of the system $\Delta\rho_{\max}$ is temperature-dependent as expressed in Eq. (2). The relationship between the consequential Rayleigh number Ra [Eq. (9)]—the ratio of the destabilizing buoyancy to the viscous and thermal diffusion—and the control parameters is shown in Fig. 9. As discussed in Sec. II B, the same Ra can be reproduced from different combinations of T_{h} and H, whereas their convective dynamics differ significantly. The latter indicates that Ra is no longer the governing parameter of the system in ice-bounded coldwater convection, highlighting the need to use the dimensional parameters.

APPENDIX C: COMPUTATION OF STREAMFUNCTION FIELDS

For mass transport, we compute the extrema of streamfunction ψ defined as

$$u = -\frac{\partial \psi}{\partial z} \quad \text{and} \quad w = \frac{\partial \psi}{\partial x}, \tag{C1}$$

Numerically, ψ is computed through the vorticity ω using the Poisson equation

$$\nabla^2 \psi = \omega = \frac{\partial w}{\partial x} - \frac{\partial u}{\partial z}, \tag{C2}$$

utilizing the successive-over-relaxation method while fulfilling the Dirichlet boundary condition, $\psi(\partial\Omega) = 0$ [51,52].

TABLE I. Fifth-order polynomial models for temperature-dependent material properties Eqs. (3a)–(3c) used in this study.

Density $\rho(T)$		Dynamic viscosity $\mu(T)$		Thermal conductivity $k(T)$	
a_i [unit]	Value	b_i [unit]	Value	c_i [unit]	Value
$a_0 = \rho(T_{\text{md}})$ [kg m^{-3}]	9.99975×10^{3}	$b_0 = \mu(T_{\text{md}})$ [Pa s]	1.56830×10^{-3}	$c_0 = k(T_{\text{md}})$ [W m^{-1} °C^{-1}]	5.65418×10^{-1}
a_1 [kg m^{-3} °C^{-1}]	-2.70561×10^{-5}	b_1 [Pa s °C^{-1}]	-5.04418×10^{-5}	c_1 [W m^{-1} °C^{-2}]	2.35301×10^{-3}
a_2 [kg m^{-3} °C^{-2}]	-7.97514×10^{-3}	b_2 [Pa s °C^{-2}]	1.30113×10^{-6}	c_2 [W m^{-1} °C^{-3}]	-2.40688×10^{-5}
a_3 [kg m^{-3} °C^{-3}]	8.33784×10^{-5}	b_3 [Pa s °C^{-3}]	-3.04195×10^{-8}	c_3 [W m^{-1} °C^{-4}]	3.33255×10^{-7}
a_4 [kg m^{-3} °C^{-4}]	-1.14606×10^{-6}	b_4 [Pa s °C^{-4}]	6.14316×10^{-10}	c_4 [W m^{-1} °C^{-5}]	-5.33687×10^{-9}
a_5 [kg m^{-3} °C^{-5}]	1.15136×10^{-8}	b_5 [Pa s °C^{-5}]	-7.53599×10^{-12}	c_5 [W m^{-1} °C^{-6}]	5.41585×10^{-11}

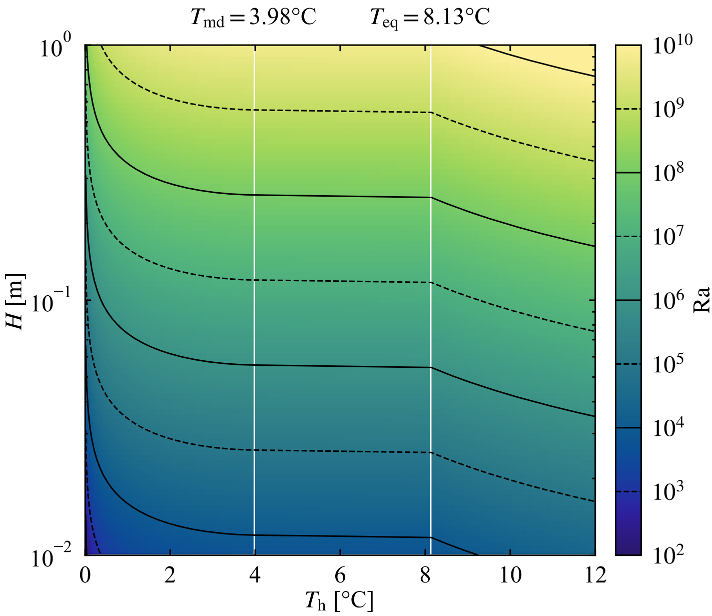

FIG. 9. Rayleigh number of ice-bounded coldwater convection.

---

[1] Y. Du, E. Calzavarini, and C. Sun, The physics of freezing and melting in the presence of flows, Nat. Rev. Phys. **6**, 676 (2024).

[2] IMBIE Team, Mass balance of the Antarctic Ice Sheet from 1992 to 2017, Nature (London) **558**, 219 (2018).

[3] IMBIE Team, Mass balance of the Greenland Ice Sheet from 1992 to 2018, Nature (London) **579**, 233 (2020).

[4] GlaMBIE Team, Community estimate of global glacier mass changes from 2000 to 2023, Nature (London) **639**, 382 (2025).

[5] A. Oberbeck, Ueber die Wärmeleitung der Flüssigkeiten bei Berücksichtigung der Strömungen infolge von Temperaturdifferenzen, Ann. Phys. **243**, 271 (1879).

[6] J. Boussinesq, *Théorie Analytique de la Chaleur: Mise en Harmonie Avec la Thermodynamique et Avec la Théorie Mécanique de la Lumière* (Gauthier-Villars, Paris, 1903), Vol. 2.

[7] G. Ahlers, S. Grossmann, and D. Lohse, Heat transfer and large scale dynamics in turbulent Rayleigh-Bénard convection, Rev. Mod. Phys. **81**, 503 (2009).

[8] G. Ahlers, E. Brown, F. F. Araujo, D. Funfschilling, S. Grossmann, and D. Lohse, Non-Oberbeck–Boussinesq effects in strongly turbulent Rayleigh–Bénard convection, J. Fluid Mech. **569**, 409 (2006).

[9] K. Sugiyama, E. Calzavarini, S. Grossmann, and D. Lohse, Flow organization in two-dimensional non-Oberbeck–Boussinesq Rayleigh–Bénard convection in water, J. Fluid Mech. **637**, 105 (2009).

[10] V. Valori, G. Elsinga, M. Rohde, M. Tummers, J. Westerweel, and T. van der Hagen, Experimental velocity study of non-Boussinesq Rayleigh–Bénard convection, Phys. Rev. E **95**, 053113 (2017).

[11] A. D. Demou and D. G. Grigoriadis, Direct numerical simulations of Rayleigh–Bénard convection in water with non-Oberbeck–Boussinesq effects, J. Fluid Mech. **881**, 1073 (2019).

[12] S. Weiss, M. S. Emran, and O. Shishkina, What Rayleigh numbers are achievable under Oberbeck–Boussinesq conditions? J. Fluid Mech. **986**, R2 (2024).

[13] E. S. Boyce, R. J. Motyka, and M. Truffer, Flotation and retreat of a lake-calving terminus, Mendenhall Glacier, southeast Alaska, USA, J. Glaciol. **53**, 211 (2007).

[14] S. Sugiyama, M. Minowa, D. Sakakibara, P. Skvarca, T. Sawagaki, Y. Ohashi, N. Naito, and K. Chikita, Thermal structure of proglacial lakes in Patagonia, JGR Earth Surface **121**, 2270 (2016).

[15] M. Leppäranta, E. Lindgren, and L. Arvola, Heat balance of supraglacial lakes in the western Dronning Maud Land, Ann. Glaciol. **57**, 39 (2016).

[16] Z. Zhong, K. Yang, and J. Lloyd, Variable property effects in laminar natural convection in a square enclosure, J. Heat Transfer. **107**, 133 (1985).

[17] M. Ishikawa, T. Hirata, and S. Noda, Numerical simulation of natural convection with density inversion in a square cavity, Numer. Heat Transfer A **37**, 395 (2000).

[18] D. Lin and M. Nansteel, Natural convection heat transfer in a square enclosure containing water near its density maximum, Int. J. Heat Mass Transf. **30**, 2319 (1987).

[19] A. Osorio, R. Avila, and J. Cervantes, On the natural convection of water near its density inversion in an inclined square cavity, Int. J. Heat Mass Transf. **47**, 4491 (2004).

[20] H. Inaba and T. Fukuda, Natural convection in an inclined square cavity in regions of density inversion of water, J. Fluid Mech. **142**, 363 (1984).

[21] S. Braga and R. Viskanta, Transient natural convection of water near its density extremum in a rectangular cavity, Int. J. Heat Mass Transf. **35**, 861 (1992).

[22] P. Mayeli and G. J. Sheard, Buoyancy-driven flows beyond the Boussinesq approximation: A brief review, Int. Commun. Heat Mass Transfer **125**, 105316 (2021).

[23] H. N. Ulloa, K. B. Winters, A. Wüest, and D. Bouffard, Differential heating drives downslope flows that accelerate mixed-layer warming in ice-covered waters, Geophys. Res. Lett. **46**, 13872 (2019).

[24] P. Léard, B. Favier, P. Le Gal, and M. Le Bars, Coupled convection and internal gravity waves excited in water around its density maximum at 4 °C, Phys. Rev. Fluids **5**, 024801 (2020).

[25] T. Hanson, M. Stastna, and A. Coutino, Stratified shear instability in the cabbeling regime, Phys. Rev. Fluids **6**, 084802 (2021).

[26] A. P. Grace, M. Stastna, K. G. Lamb, and K. A. Scott, Asymmetries in gravity currents attributed to the nonlinear equation of state, J. Fluid Mech. **915**, A18 (2021).

[27] J. Olsthoorn, E. W. Tedford, and G. A. Lawrence, The cooling box problem: Convection with a quadratic equation of state, J. Fluid Mech. **918**, A6 (2021).

[28] L.-A. Couston and M. Siegert, Dynamic flows create potentially habitable conditions in Antarctic subglacial lakes, Sci. Adv. **7**, eabc3972 (2021).

[29] A. P. Grace, M. Stastna, K. G. Lamb, and K. A. Scott, Gravity currents in the cabbeling regime, Phys. Rev. Fluids **8**, 014502 (2023).

[30] R. Yang, C. J. Howland, H.-R. Liu, R. Verzicco, and D. Lohse, Bistability in radiatively heated melt ponds, Phys. Rev. Lett. **131**, 234002 (2023).

[31] D. J. M. Allum and M. Stastna, Simulations of buoyant flows driven by variations in solar radiation beneath ice cover, Phys. Rev. Fluids **9**, 063501 (2024).

[32] G. O. Hughes and R. W. Griffiths, Horizontal convection, Annu. Rev. Fluid Mech. **40**, 185 (2008).

[33] B. Gayen, R. W. Griffiths, G. O. Hughes, and J. A. Saenz, Energetics of horizontal convection, J. Fluid Mech. **716**, R10 (2013).

[34] O. Shishkina, S. Grossmann, and D. Lohse, Heat and momentum transport scalings in horizontal convection, Geophys. Res. Lett. **43**, 1219 (2016).

[35] C. S. Ng, A. Ooi, D. Lohse, and D. Chung, Vertical natural convection: Application of the unifying theory of thermal convection, J. Fluid Mech. **764**, 349 (2015).

[36] O. Shishkina, Momentum and heat transport scalings in laminar vertical convection, Phys. Rev. E **93**, 051102(R) (2016).

[37] E. W. Lemmon, I. H. Bell, M. L. Huber, and M. O. McLinden, Thermophysical properties of fluid systems, in *NIST Standard Reference Database 69: NIST Chemistry WebBook*, edited by P. Linstrom and W. Mallard (National Institute of Standards and Technology, Gaithersburg, MD, 2024), https://webbook.nist.gov/chemistry/fluid/.

[38] D. Noto and H. N. Ulloa, Melting dynamics of freely floating ice in calm waters, Sci. Adv. **12**, eady3529 (2026).

[39] H. N. Ulloa, A. Wüest, and D. Bouffard, Mechanical energy budget and mixing efficiency for a radiatively heated ice-covered waterbody, J. Fluid Mech. **852**, R1 (2018).
[40] S. Musman, Penetrative convection, J. Fluid Mech. **31**, 343 (1968).
[41] Z. Wang, E. Calzavarini, C. Sun, and F. Toschi, How the growth of ice depends on the fluid dynamics underneath, Proc. Natl. Acad. Sci. USA **118**, e2012870118 (2021).
[42] D. Xu, R. Yang, R. Verzicco, and D. Lohse, Aspect ratio effect on side and basal melting in fresh water, J. Fluid Mech. **1010**, A40 (2025).
[43] R. A. Fine and F. J. Millero, Compressibility of water as a function of temperature and pressure, J. Chem. Phys. **59**, 5529 (1973).
[44] B. Gebhart and J. C. Mollendorf, Buoyancy-induced flows in water under conditions in which density extrema may arise, J. Fluid Mech. **89**, 673 (1978).
[45] E. C. Carmack, Combined influence of inflow and lake temperatures on spring circulation in a riverine lake, J. Phys. Oceanogr. **9**, 422 (1979).
[46] G. Estay, D. Noto, and H. N. Ulloa, Under-ice convective regimes driven by sunlight and sediment temperature control water–ice heat flux, PNAS Nexus **5**, pgag045 (2026).
[47] A. Arakawa and V. R. Lamb, Computational design of the basic dynamical processes of the UCLA General Circulation Model, in *General Circulation Models of the Atmosphere*, Methods in Computational Physics: Advances in Research and Applications, Vol. 17, edited by J. Chang (Elsevier, New York, 1977), pp. 173–265.
[48] A. A. Amsden and F. H. Harlow, A simplified MAC technique for incompressible fluid flow calculations, J. Comput. Phys. **6**, 322 (1970).
[49] D. Noto and H. N. Ulloa, Numerical code, Two-dimensional direct numerical simulation of thermal convection in water with actual material properties, Zenodo, 2025, https://doi.org/10.5281/zenodo.17189478.
[50] O. Shishkina, R. J. Stevens, S. Grossmann, and D. Lohse, Boundary layer structure in turbulent thermal convection and its consequences for the required numerical resolution, New J. Phys. **12**, 075022 (2010).
[51] D. Noto, T. Terada, T. Yanagisawa, T. Miyagoshi, and Y. Tasaka, Developing horizontal convection against stable temperature stratification in a rectangular container, Phys. Rev. Fluids **6**, 083501 (2021).
[52] D. Noto, H. N. Ulloa, T. Yanagisawa, and Y. Tasaka, Stratified horizontal convection, J. Fluid Mech. **970**, A21 (2023).
[53] S. Zilitinkevich, K. Kreiman, and A. Y. Terzhevik, The thermal bar, J. Fluid Mech. **236**, 27 (1992).
[54] P. R. Holland and A. Kay, A review of the physics and ecological implications of the thermal bar circulation, Limnologica **33**, 153 (2003).
[55] B. O. Tsydenov, A numerical study of the thermal bar in shallow water during the autumn cooling, J. Great Lakes Res. **45**, 715 (2019).
[56] Z. Virag, M. Živić, and A. Galović, Influence of natural convection on the melting of ice block surrounded by water on all sides, Int. J. Heat Mass Transf. **49**, 4106 (2006).
[57] A. Sedaghatkish, F. Doumenc, P.-Y. Jeannin, and M. Luetscher, Modelling the effect of free convection on permafrost melting rates in frozen rock clefts, Cryosphere **18**, 4531 (2024).
[58] W. Tong and J. N. Koster, Natural convection of water in a rectangular cavity including density inversion, Int. J. Heat Fluid Flow **14**, 366 (1993).
[59] T. Wei and J. N. Koster, Density inversion effect on transient natural convection in a rectangular enclosure, Int. J. Heat Mass Transf. **37**, 927 (1994).
[60] M. A. Hossain and D. S. Rees, Natural convection flow of water near its density maximum in a rectangular enclosure having isothermal walls with heat generation, Heat Mass Transfer **41**, 367 (2005).
[61] S. Weady, J. Tong, A. Zidovska, and L. Ristroph, Anomalous convective flows carve pinnacles and scallops in melting ice, Phys. Rev. Lett. **128**, 044502 (2022).
[62] K. B. Winters, H. N. Ulloa, A. Wüest, and D. Bouffard, Energetics of radiatively heated ice-covered lakes, Geophys. Res. Lett. **46**, 8913 (2019).
[63] S. E. Hampton, M. V. Moore, T. Ozersky, E. H. Stanley, C. M. Polashenski, and A. W. Galloway, Heating up a cold subject: Prospects for under-ice plankton research in lakes, J. Plankton Res. **37**, 277 (2015).

[64] L. B. Knoll, S. Sharma, B. A. Denfeld, G. Flaim, Y. Hori, J. J. Magnuson, D. Straile, and G. A. Weyhenmeyer, Consequences of lake and river ice loss on cultural ecosystem services, Limnol. Oceanogr. Lett. **4**, 119 (2019).

[65] R. I. Woolway, L. Huang, S. Sharma, S.-S. Lee, K. B. Rodgers, and A. Timmermann, Lake ice will be less safe for recreation and transportation under future warming, Earth's Future **10**, e2022EF002907 (2022).

[66] S. E. Hampton, S. M. Powers, H. A. Dugan, L. B. Knoll, B. C. McMeans, M. F. Meyer, C. M. O'Reilly, T. Ozersky, S. Sharma, D. C. Barrett, *et al.*, Environmental and societal consequences of winter ice loss from lakes, Science **386**, eadl3211 (2024).